photonics

MDPI

Article

Perovskite $MAPbBr_2I$ All-Optical Synapses for Dynamic Pattern Recognition and Diffractive Neuromorphic Computing

Yang Fang [1,2], Yitong Wu [1], Qing Hou [1,2,*] and Xi Chen [1,2,*]

[1] School of Artificial Intelligence Science and Technology, University of Shanghai for Science and Technology, Shanghai 200093, China; 232200367@st.usst.edu.cn (Y.F.)
[2] Institute of Photonic Chips, University of Shanghai for Science and Technology, Shanghai 200093, China
* Correspondence: qinghou@usst.edu.cn (Q.H.); xichen@usst.edu.cn (X.C.)

Abstract

Conventional optoelectronic synapses rely on electrical signals for core operations, resulting in complex circuitry, limited response speed, and energy inefficiency. Herein, an all-optical synapse based on perovskite $MAPbBr_2I$ is developed that directly converts optical stimuli into transmittance responses that mimic fundamental synaptic plasticity, including paired-pulse facilitation, short- and long-term memory, and learning. By using the dynamic transmittance response as input to an artificial neural network, high-accuracy dynamic pattern recognition of sequential characters is achieved. Furthermore, the optically controlled transmittance states are successfully integrated as programmable weights into a diffractive neural network, enabling all-optical classification of MNIST handwritten digits with an accuracy of 89%. This fully optical architecture, which eliminates electronic components and complex circuits, offers a promising pathway toward high-speed, energy-efficient vision systems by fundamentally circumventing the von Neumann bottleneck.

Keywords: all-optical artificial synapse; perovskite; dynamic recognition; diffractive neural network

1. Introduction

The advent of the artificial intelligence era has placed higher demands on the real-time performance and environmental adaptability of information processing systems [1–4]. Especially in complex signal recognition tasks, such systems must be capable of efficient perception and response to multimodal environmental information [5–8]. Against this backdrop, optoelectronic synapses [9–11] can directly utilize optical signals to mimic neural behaviors [12–16], demonstrating great potential in feature recognition and dynamic responses to environmental signals such as light and electricity [17–19], and thus providing a new pathway for the construction of high-efficiency neuromorphic systems [20–24]. However, most existing optoelectronic synapses still cannot break their dependence on electrical signals during core computing processes [25,26]. Their processing procedures require complex circuits and do not support wireless transmission of response signals, resulting in significant bottlenecks in response speed and energy efficiency [27]. Therefore, the development of devices capable of all-optical neuromorphic computing has become urgent.

To address this limitation, we develop an all-optical synapse based on perovskite $MAPbBr_2I$, in which optical transmittance is modulated by light pulses. Light-driven synaptic behaviours, including paired-pulse facilitation (PPF), short-term memory (STM),

Check for updates

Received: 21 February 2026
Revised: 20 March 2026
Accepted: 26 March 2026
Published: 27 March 2026

Copyright: © 2026 by the authors. Licensee MDPI, Basel, Switzerland. This article is an open access article distributed under the terms and conditions of the Creative Commons Attribution (CC BY) license.

long-term memory (LTM), and learning experience [28–33], can be mimicked. By simulating an artificial neural network (ANN) using the transmittance responses of $MAPbBr_2I$ synapses as inputs, high-performance dynamic pattern recognition can be demonstrated. Moreover, once the synapses are utilized in the diffractive layer of an optical neuromorphic computing architecture, transmittance synaptic weights with 25-level precision in the diffractive neural network (DNN) are achieved, thus enabling all-optical pattern classification with an accuracy of 89%. These findings pave the way for an all-optical neuromorphic vision system. By fundamentally circumventing the memory wall, such a system transitions a conceptual blueprint to a tangible reality, making it a highly attractive prospect.

2. Materials and Methods

Preparation of $MAPbBrI_2$ perovskite films. Lead bromide ($PbBr_2$, 99.999%) and methylammonium iodide (MAI, 99.999%) were purchased from Sigma-Aldrich (St. Louis, MO, USA). N,N-Dimethylformamide (DMF, 99.5%) was purchased from Sinopharm Chemical Reagent Co., Ltd. (Shanghai, China). MAI and $PbBr_2$ were dissolved in 1000 μL of DMF, stirred at room temperature for 2 h, and then filtered. Then, the as-prepared solution was spin-coated on the substrate at 5000 rpm for 120 s in a glove box. The perovskite precursor solution was introduced into a nitrogen-filled glove box, spun at 3000 rpm for 100 s to spin-coat a perovskite film onto a glass substrate, and then annealed at 70 °C for 1 h.

Characterization of $MAPbBrI_2$ all-optical synapses. X-ray diffraction (XRD) analysis was performed using a Bruker AXS D8-ADVANCE diffractometer(Bruker AXS GmbH, Karlsruhe, Germany) operated at 40 kV and 40 mA. The surface morphology and elemental composition of the samples were studied using a Nova NanoSEM 450 (FEI, Thermo Fisher Scientific, Waltham, MA, USA) at an accelerating voltage of 3 kV, employing field-emission scanning electron microscopy (SEM) and energy-dispersive X-ray (EDX) spectrometry. In addition, the film morphology was examined using atomic force microscopy (AFM) on a Dimension Icon (Bruker, Billerica, MA, USA). Absorption and transmission spectra of the synapses were measured using an ultraviolet spectrophotometer (Shimazu UV-2600i/2700i, Shimadzu Corporation, Kyoto, Japan) in the wavelength range of 300 nm to 800 nm. Real-time transmittance measurement was conducted using a self-constructed testing system. This system comprises a 365 nm LED light source to trigger transmittance changes, and the transmittance was measured using a high-speed CMOS spectrometer (Avaspec-ULS2048CL-EVO, Avantes BV, Apeldoorn, The Netherlands).

Dynamic pattern recognition. We defined ΔT as 5% of the pixel grayscale value 255. Next, a direct proportionality between grayscale value and ΔT was established to obtain images for pattern recognition. An ANN was implemented, comprising a 5-neuron input layer for temporal feature extraction, a 20-cell long short-term memory layer for sequence modeling, and a 2-neuron output layer with SoftMax activation. The model was optimized using the Adam optimizer ($\alpha = 1 \times 10^{-3}$, $\beta_1 = 0.9$, $\beta_2 = 0.999$) and small-batch training (batch size = 2) to minimize cross-entropy loss.

Diffractive neuromorphic computing. A DNN structure was trained on 60,000 images from the MNIST and Fashion-MNIST datasets. Subsequently, 10,000 test images were used to compute classification accuracy for 10 handwritten digits and fashion products. The wavelength of the input images is 633 nm. The DNN employed backpropagation with an Adam optimizer to update the weights, using a learning rate of 0.0001 and a batch size of 10.

3. Results

Bionic synapses act as the communication junctions among neurons, enabling the transmission of electrical or chemical signals throughout the brain's neural network. Inspired by this, we fabricated a perovskite $MAPbBr_2I$ all-optical artificial synapse that converts optical stimuli into optical transmittance signals, thereby enabling neural network perception and computation. A dihydrated perovskite ($(MA)_4PbBr_4I_2{\cdot}2H_2O$, dihydrated $MAPbBr_2I$) solution is synthesized with $PbBr_2$ and MAI. The precursor solution is dispensed onto a glass substrate by spin coating and annealed to enhance crystallinity and reduce intrinsic defects [34,35]. UV light illuminating the all-optical synapse can drive water molecules out of the lattice, thereby decreasing transmittance. Humidity governs rehydration and enables reversible optical modulation. This mechanism directly converts light stimuli into tunable transmittance states, mimicking synaptic plasticity without the use of electronic components. (Figure 1a). A SEM image of the dihydrated $MAPbBr_2I$ film (Figure 1b) indicates that the surface presents a dense and uniform morphology. An EDX spectrum of the $(MA)_4PbBr_4I_2{\cdot}2H_2O$ film, present in Figure 1c, confirms the chemical stoichiometry of a Pb:Br:I ratio approximating 1:4:2. XRD patterns in Figure 1d imply a structural change where a tetragonal phase of dihydrated $MAPbBr_2I$ transforms into a cubic phase of $MAPbBr_2I$ [36,37]. An AFM image (Figure S1) shows a surface roughness (Ra) of 54.765 nm and clear grain boundaries. As shown in Figure S2, the absorption characteristics of the dihydrated $MAPbBr_2I$ within a wavelength range from 300 to 800 nm show significant modulation under UV stimulation. Before optical treatment, a strong absorption peak at 365 nm is observed, attributable to the band-edge transition [34]. The transmission spectra (Figure 1e) exhibit broad transmittance tuning across 600 nm, ranging from 75% to 10%. Compared with other perovskites, the dihydrated $MAPbBr_2I$ has a broader transmittance modulation than $MAPbBr_3$ (Figure S3). Though the modulation value is a bit lower than that of $MAPbI_3$, the light stability of $MAPbBr_2I$ is dramatically higher than that of $MAPbI_3$ due to the existence of Br vacancies. With its optimal balance between broadband transmittance modulation and environmental stability (Figure S4), the dihydrated $MAPbBr_2I$ is a highly promising candidate for all-optical neuromorphic computing.

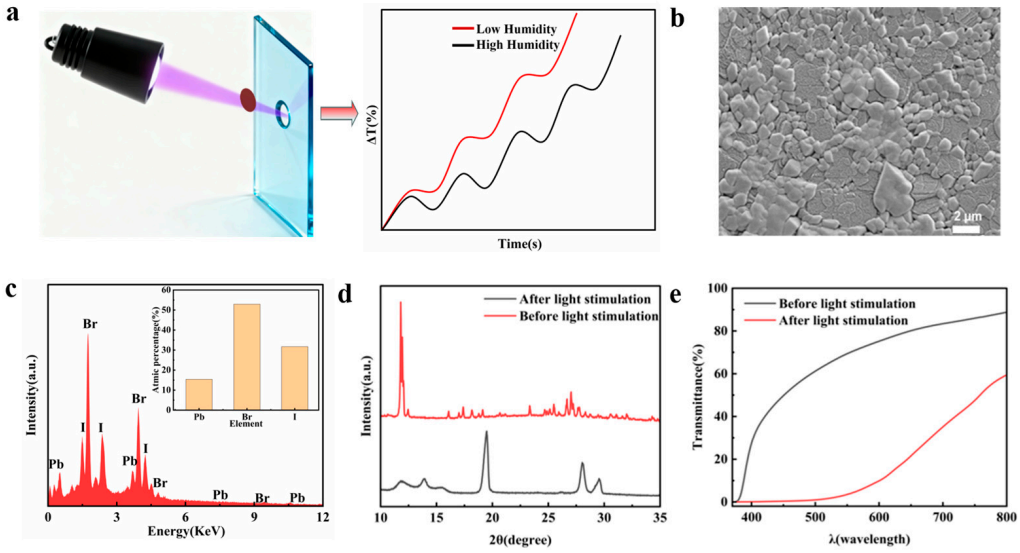


Figure 1. (**a**) Light-driven transmittance responses of a $MAPbBr_2I$ all-optical synapse under different humidities. (**b**) A SEM image of a dihydrated $MAPbBr_2I$ film. (**c**) An EDX spectrum of a dihydrated $MAPbBr_2I$ film. Inset: Element composition of the film. XRD patterns (**d**) and transmission spectra (**e**) of a dihydrated $MAPbBr_2I$ film before and after 383 mW 365 nm pulse illumination for 1 h.

During learning and memory in the human brain, the information initially received forms a memory trace that is temporarily stored in the hippocampus, and the memory fades over time through signal transmission at biologically realistic synapses [38]. To simulate the behavior, a dihydrated $MAPbBr_2I$ film is illuminated with a 365 nm pulse to measure the change in transmittance (ΔT) at 600 nm. The ΔT increases during illumination and gradually fades after pulse termination (Figure 2a). Moreover, the all-optical synapse can mimic the brain's adaptive learning by tuning light and environmental parameters. These adjustments simulate biological plasticity, enabling devices to process information and form memories, analogous to neural connections [28]. The all-photonic synapse can be stimulated by increasing the duration and power of a light pulse. The ΔT turns higher as the duration of a 365 nm pulse rises from 15 to 55 s (Figure 2b). Increasing the pulse power from 128 to 383 mW also increases ΔT (Figure 2c).

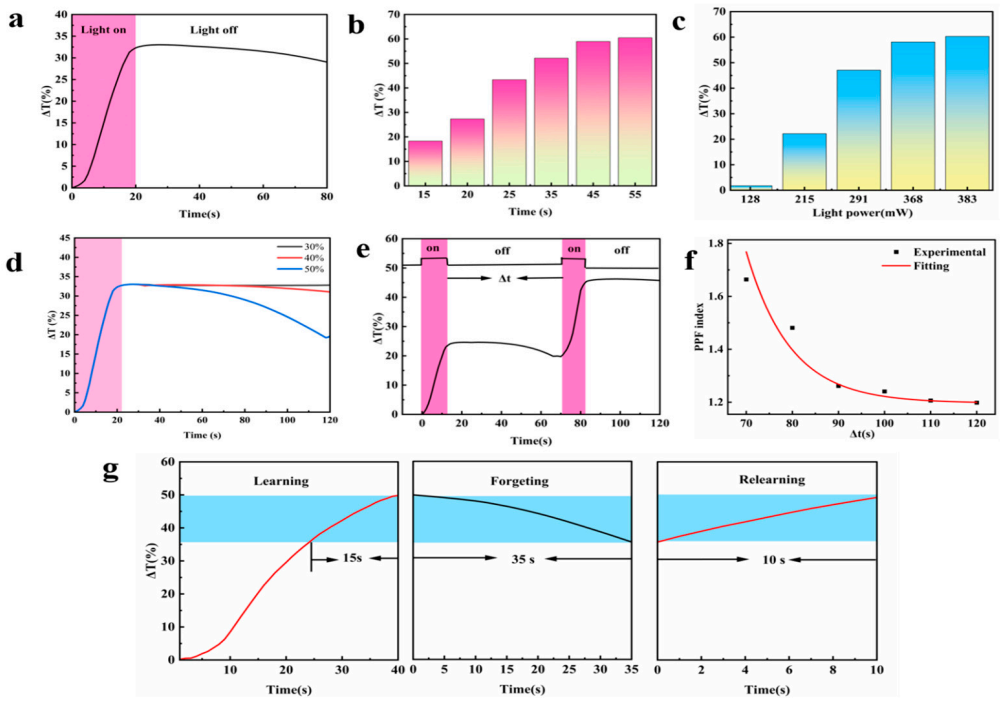


Figure 2. (**a**) ΔT changes during and after 383 mW 365 nm pulse illumination under 50% RH. (**b**) ΔT values induced by 383 mW 365 nm pulse illumination at different times. The standard deviation is within 0.8%. (**c**) ΔT values induced by 365 nm 55 s pulse illumination with different powers. The standard deviation is within 0.8%. (**d**) ΔT changes during and after 383 mW 365 nm pulse illumination under various RH values. (**e**) ΔT changes under two 383 mW 365 nm pulses with an interval of 60 s under 50% RH. (**f**). The relationship between PPF index and interval times. The standard deviation of the PPF index is within 0.07. (**g**) Learning experience obtained using two 368 mW, 365 nm pulses separated by 35 s at 75% RH.

In addition to the plasticity, flexible control of synaptic memory states, such as STM and LTM, is critical for advancing neuromorphic functionality. For the $MAPbBr_2I$ all-optical artificial synapse, the transition between STM and LTM can be realized by the tuning of relative humidity (RH). As shown in Figure 2d, after the light pulse ends, ΔT exhibits a pronounced RH dependence. The ΔT degrades rapidly at 60% RH and remains nearly stable at 30% RH. This distinct behavior arises from the permeation of water molecules into the crystal lattice, which is regulated by humidity. At high RH, increased water molecules facilitate structural rehydration, thereby accelerating the ΔT degradation. Conversely, reduced water content at low RH impedes rehydration, thereby prolonging ΔT retention [34].

PPF is a typical behavior of biological synapses, where the second light stimulus exhibits a higher synaptic response than the first light stimulus [29]. Figure 2e represents the PPF behavior of the all-optical synapse. The ΔT is measured during the two 365 nm pulses separated by a 60 s interval. The ΔT achieved by the second light pulse (A_2) is more obvious than that after the first one (A_1). Figure 2f shows the relationship between PPF and the interval of light stimulation. As the interval time increases from 60 to 110 s, the PPF index defined by A_2/A_1 decreases from 1.40 to 1.20, indicating that PPF is inversely proportional to the interval time. The PPF index decay defined by A_2/A_1 can be described by a double exponential function:

$$PPF = 1 + C_1 \exp\left(-\frac{\Delta t}{\tau_1}\right) + C_2 \exp\left(-\frac{\Delta t}{\tau_2}\right) \quad (1)$$

where Δt represents the interval time, C_1 (C_2) is the initial facilitation amplitude of the fast (slow) decay phase, and τ_1 (τ_2) are the characteristic relaxation times of the fast (slow) decay. The fitted parameters yield τ_1 = 1.5 s and τ_2 = 23 s. The τ_2 value is one order of magnitude larger than τ_1, which is consistent with the decay kinetics of PPF in biological synapses [30,31].

Biologically, initial learning requires the greatest effort, with memory traces fading gradually over time. However, relearning is significantly more efficient, demanding less effort to regain prior proficiency [30,31]. The learning experience can also be mimicked by the $MAPbBr_2I$ all-optical synapse. As shown in Figure 2g, during the first learning phase, 15 s were required to increase ΔT from 36% to 49%. After a period of forgetting, only 10 s were sufficient to achieve the same level of enhancement during relearning. This accelerated relearning phenomenon is attributed to incomplete structural recovery after the first learning, whereby the film remains in a metastable state and retains structural traces of the previous dehydration process. This metastable state lowers the energy barrier to subsequent phase transitions, accelerating the efflux of water molecules upon re-illumination and thereby yielding a faster optical response [34].

Due to synaptic plasticity in $MAPbBr_2I$ all-optical synapses, characteristic ΔT responses are generated under varying optical-pulse parameters and used as inputs to neuromorphic computing for dynamic pattern recognition. We simulated a 5 × 5 all-optical synapse array. Letters of selected words were successively projected onto the 5 × 5 array during 383 mW 365 nm UV light pulse illumination for 5 s, causing transmittance modulation in the corresponding synapses (Figure 3a). The words used in the experiment included "NEW", "ANT", "MAN", "PAN", and "ON" (Figure S5). Next, the ΔT values of each synapse are proportionally converted into a grayscale value, with 5% of the ΔT corresponding to a grayscale value of 255. A specific 5 × 5 grayscale image for each word is generated, then added to random noise and fed into an ANN for recognition. The implemented ANN features a three-layer architecture, including a 5-neuron input layer, a 20-cell long LSTM layer, and a 2-neuron output layer with SoftMax activation. For training, the model was optimized using the Adam algorithm. A small-batch strategy (batch size of 2) was employed to minimize the cross-entropy loss.

The grayscale images for words "NEW", "ANT", "MAN", "PAN", and "ON" are shown in Figure 4b, in which the pulse and interval times are set to 2 s, and RH is 50% (Figure 3b). Since each word corresponds to different optical pulse irradiation parameters for the synaptic array, the grayscale image generated for each word is also completely different. Figure 3c presents the ANN-based recognition accuracy and loss function, showing that the network achieved 100% accuracy after 200 training epochs. The confusion matrix (Figure 3d) and output energy distribution (Figure S6) also demonstrate that the all-optical synapse can efficiently and accurately recognize patterns with the assistance of an ANN.

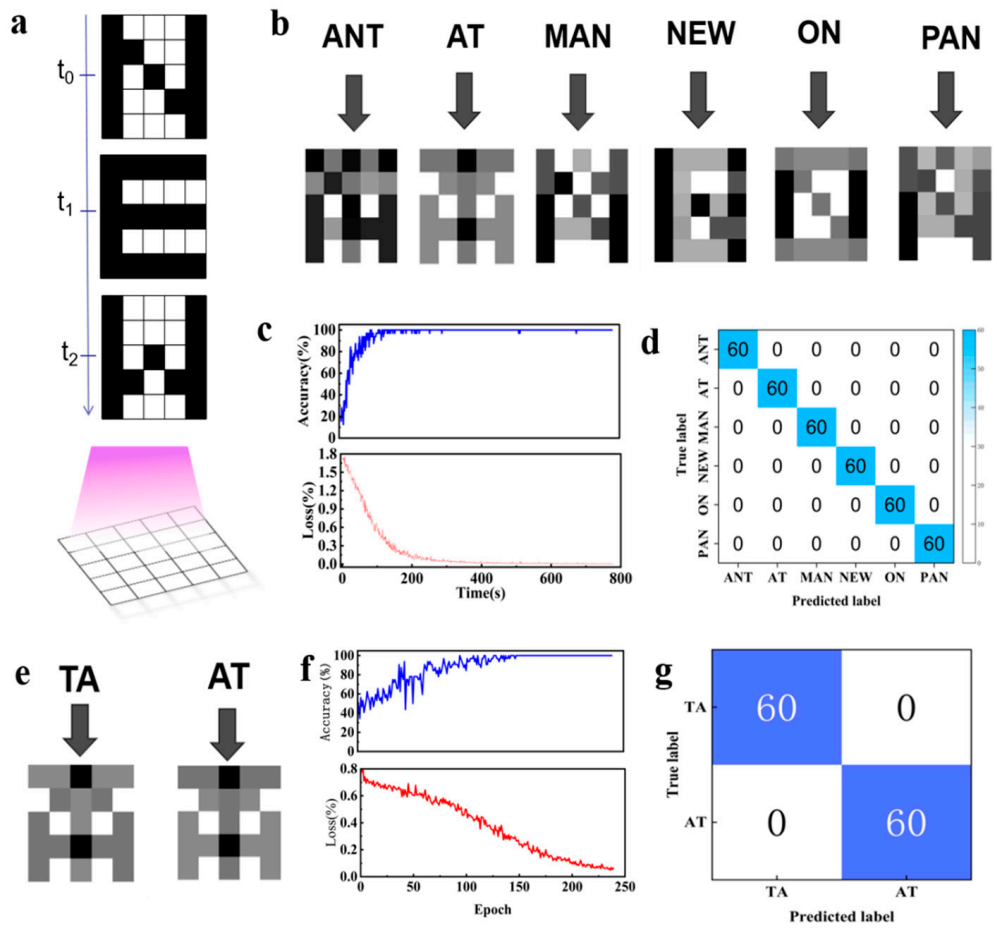


Figure 3. (**a**) Word "NEW" projected onto the 5 × 5 all-optical synapse array during 365 nm UV light pulse illumination. (**b**) Grayscale images generated for the words "ANT", "AT", "MAN", "NEW", "ON", and "PAN". (**c**) Accuracy and loss for the recognition of the words "ANT", "AT", "MAN", "NEW", "ON", and "PAN". (**d**) The confusion matrix for the recognition of the words "ANT", "AT", "MAN", "NEW", "ON", and "PAN". (**e**) Grayscale images generated for the words "TA" and "AT". (**f**) Accuracy and loss for the recognition of the words "TA" and "AT". (**g**) The confusion matrix for the recognition of the words "TA" and "AT".

Additionally, this neural network architecture can dynamically recognize words that share the same letters in different orders. To address a recognition of words "TA" and "AT", 365 nm pulses were first used to project 'T' onto the corresponding synapses for 2 s, waiting for 2 s before projecting 'A' to generate a grayscale image for "TA". For the image generation for "AT", the same pathway was used to project 'A' and then 'T' (Figure 3e). Due to the STM under high RH (50%), the ΔT of synapses irradiated during the first exposure but not during the second exposure shows a significant decrease, resulting in a difference between the images of the two words. Once these images are input into an ANN, the training accuracy reaches 100% at the 200th epoch, as shown in Figures 3f,g and S7). These results imply that high-performance dynamic pattern recognition can be achieved through ANN-based neuromorphic computing using optical input from artificial synapses.

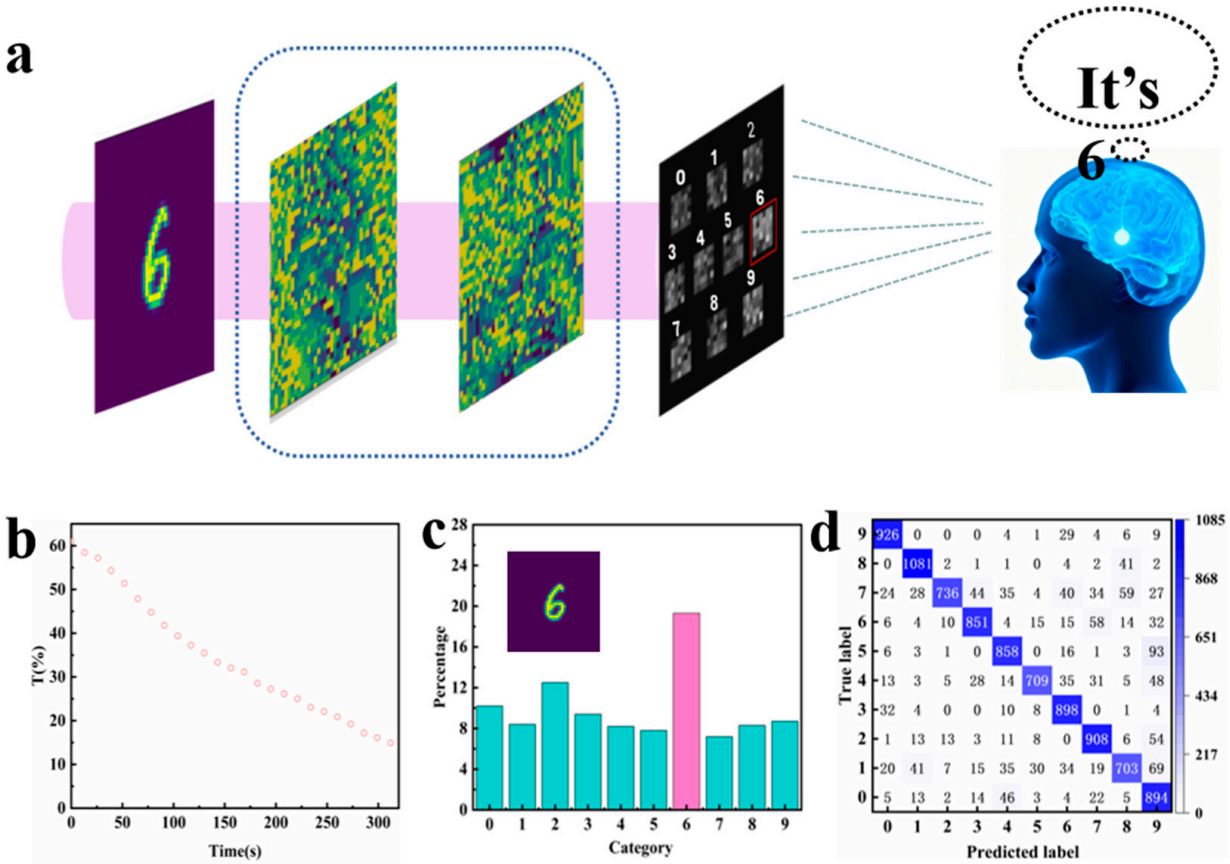


Figure 4. (**a**). Schematic illustration of an all-optical synapse integrated with a DNN for recognizing MNIST handwritten digits. (**b**) Transmittance weight states of the all-optical synapse. The standard deviation is within 0.8%. (**c**) The energy distribution for an input of digit "6". (**d**). The confusion matrix for recognizing MNIST handwritten digits.

A diffractive neural network (DNN) is an optical neuromorphic computing framework that processes data at the speed of light, offering advantages of high-throughput data processing and low energy consumption [39–41]. It realizes the connection between diffraction layers based on the Rayleigh–Sommerfeld diffraction. Specifically, neurons are connected via secondary waves, and the amplitude or phase of these waves is modulated by the input field from the previous layer and by local transmission. The transformation from an input optical field vector $I = [I_1, I_2, \ldots, I_m]^T$ to an output vector $I' = [I'_1, I'_2, \ldots I'_n]^T$ through a layer of an all-optical synapse array is described by:

$$D\begin{pmatrix} T_1 \\ \vdots \\ T_i \end{pmatrix} = \begin{bmatrix} T_{1,1} & \cdots & T_{1,n} \\ \vdots & \ddots & \vdots \\ T_{m,1} & \cdots & T_{m,n} \end{bmatrix} \quad (2)$$

$$\begin{bmatrix} I'_1 \\ \vdots \\ I'_n \end{bmatrix} = \begin{bmatrix} T_{1,1} & \cdots & T_{1,n} \\ \vdots & \ddots & \vdots \\ T_{m,1} & \cdots & T_{m,n} \end{bmatrix} \begin{bmatrix} I_1 \\ \vdots \\ I_m \end{bmatrix} \quad (3)$$

where $T_1 - T_i$ denote the transmittance weight matrix (each element is one of 80 discrete values) and D represents the diffraction propagation function. This operation inherently performs the weighted summation in parallel. The multiplication $T_{i,j}I_j$ is realized by modulating the amplitude of the input field through the synaptic element, while the summation is physically implemented by the coherent superposition of light waves at the output plane.

The various transmittance weights can be achieved by illuminating $MAPbBr_2I$ all-optical synapses with 365 nm pulses under low RH (30%). The two diffraction layers are composed of 40 × 40 μm neurons (Figure 4a). The transmittance weights, obtained by illuminating the synapse with a 383 mW 365 nm pulse at different times and 30% RH, range from 61% to 15%. These values correspond to 25 distinct programmable weight states (Figure 4b). Next, these transmittance weights are incorporated into the DNN architecture to perform classification on the MNIST handwritten digits dataset. As shown in Figure 4c, digit "6" was input into the synapse-based diffraction layer. The resulting light-intensity distribution was highest at the sixth detector (Figure 4c), thereby confirming the correct identification. The DNN was trained on 60,000 handwritten digit images from the MNIST dataset and tested on 10,000 images per digit. The confusion matrix (Figure 4d) indicates successful classification, with a test accuracy of 89%. This optical neuromorphic computing technology, based on all-optical synapses, provides a circuit-free, cost-effective, and ultrafast alternative to conventional electronic approaches. Its simplicity, high processing speed, and strong environmental adaptability make it well-suited for edge artificial intelligence, adaptive optical preprocessing, robust vision systems, and reconfigurable holography, particularly in resource-limited settings.

As a circuit-free, low-cost, zero-processing-energy, and ultrafast-processing alternative, the all-optical synapse presents a compelling solution for neuromorphic computing. While its switching speed and modulation depth currently are lower than those of optoelectronic synapses, its inherent simplicity, high processing speed, and outstanding environmental adaptability make it well-suited for resource-constrained applications, including edge artificial intelligence, adaptive optical preprocessing, and robust vision systems.

4. Conclusions

This work demonstrates all-optical neuromorphic devices based on perovskite $MAPbBr_2I$. Under UV illumination, the devices exhibit broadband optical modulation, achieving 65% transmittance at 600 nm. Through the light-driven plasticity of optical transmittance responses, the all-optical synapses successfully emulate key synaptic behaviors, including PPF indices that range from 1.40 to 1.20 with relaxation times, transmittance tuning controlled by pulse duration and power, STM-LTM transition through the humidity adjustment, and an accelerated relearning process, which is 33% faster than initial learning. Based on the plasticity, dynamic pattern recognition via an ANN achieves 100% accuracy for sequential characters. Furthermore, when programmed as analog weights in a diffractive neural network, the system classifies MNIST handwritten digits with 89% accuracy over 10,000 test images. These results validate a fully optical, circuit-free computing pathway that offers a promising solution for high-speed, low-power neuromorphic vision.

Supplementary Materials: The following supporting information can be downloaded at: https://www.mdpi.com/article/10.3390/photonics13040328/s1, Figure S1: An AFM image of a dihydrated $MAPbBr_2I$ film; Figure S2: Absorption spectra of a dihydrated $MAPbBr_2I$ film before and after 383 mW 365 nm pulse illumination for 1 h; Figure S3: Transmission spectra of dihydrated $MAPbI_3$ (a), $MAPbBr_2I$ (b), and $MAPbI_3$ (c) films before and after 383 mW 365 nm pulse illumination for 1 h; Figure S4: Time-dependent transmission change responses of dihydrated $MAPbBr_3$, $MAPbI_3$ and $MAPbBr_2I$ films during and after 60 s 383 mW 365 nm pulse illumination; Figure S5: Words "ANT", "AT", "MAN", "ON", and "PAN" projected onto the 5 × 5 all-optical synapse array during 365 nm UV light pulse illumination; Figure S6: The confusion matrix for the recognition of the words "ANT" (a), "AT" (b), "MAN" (c), "NEW" (d), "ON" (e), and "PAN" (f); Figure S7: The confusion matrix for the recognition of the words "TA" (a) and "AT" (b).

Author Contributions: Y.F.: Investigation, Writing. Y.W.: Software, Writing. Q.H.: Writing, Editing, Supervision. X.C.: Conceptualization, Writing, Editing, Supervision. All authors have read and agreed to the published version of the manuscript.

Funding: This work was supported by the National Natural Science Foundation of China (Grant No. 11974247 and 52401057).

Institutional Review Board Statement: Not applicable.

Informed Consent Statement: Not applicable.

Data Availability Statement: The data that support the findings of this study are available on request from the corresponding author. The data are not publicly available due to privacy or ethical restrictions.

Conflicts of Interest: The authors declare no conflicts of interest.

Abbreviations

MNIST	Modified national institute of standards and technology database
PPF	Paired-pulse facilitation
STM	Short-term memory
LTM	Long-term memory
ANN	Artificial neural network
DNN	Diffractive neural network
XRD	X-ray diffraction
SEM	Scanning electron microscopy
EDX	Energy-dispersive x-ray
AFM	Atomic force microscopy
UV	Ultraviolet spectrophotometer
CMOS	Complementary metal-oxide semiconductor
LED	Light emitting diode
RH	Relative humidity
$PbBr_2$	Lead bromide
MAI	Methylammonium
DMF	N-dimethylformamide
FEI	Thermo Fisher Scientific

References

1. Shen, Y.; Harris, N.C.; Skirlo, S.; Prabhu, M.; Baehr-Jones, T.; Hochberg, M.; Sun, X.; Zhao, S.; Larochelle, H.; Englund, D. Deep learning with coherent nanophotonic circuits. *Nat. Photonics* **2017**, *11*, 41–48. [CrossRef]
2. Hinton, G.E.; Salakhutdinov, R.R. Reducing the dimensionality of data with neural networks. *Science* **2006**, *313*, 504–507. [CrossRef]
3. Feldmann, J.; Youngblood, N.; Wright, C.D.; Bhaskaran, H.; Pernice, W.H.P. All-optical spiking neurosynaptic networks with self-learning capabilities. *Nature* **2019**, *569*, 208–214. [CrossRef]
4. Mennel, L.; Symonowicz, J.; Wachter, S.; Polyushkin, D.K.; Molina-Mendoza, A.J.; Mueller, T. Ultrafast machine vision with 2D material neural network image sensors. *Nature* **2020**, *579*, 62–66. [CrossRef] [PubMed]
5. Yao, P.; Wu, H.; Gao, B.; Tang, J.; Zhang, Q.; Zhang, W.; Yang, J.J.; Qian, H. Fully hardware-implemented memristor convolutional neural network. *Nature* **2020**, *577*, 641–646. [CrossRef]
6. Wang, C.; Mao, G.Q.; Huang, M.; Huang, E.; Zhang, Z.; Yuan, J.; Cheng, W.; Xue, K.H.; Wang, X.; Miao, X. HfO_x/AlO_y superlattice-like memristive synapse. *Adv. Sci.* **2022**, *9*, 2201446.
7. Yang, H.; Zhang, Y.; Hu, F.; Li, Z.; Wu, D.; Chen, X. Comprehensively modulated sub-attojoule operated optoelectronic synapses for image encryption and inpainting. *ACS Appl. Mater. Interfaces* **2024**, *16*, 57804–57814. [CrossRef]
8. Markram, H.; Muller, E.; Ramaswamy, S.; Reimann, M.W.; Abdellah, M.; Sanchez, C.A.; Ailamaki, A.; Alonso-Nanclares, L.; Antille, N.; Arsever, S. Reconstruction and simulation of neocortical microcircuitry. *Cell* **2015**, *163*, 456–492. [CrossRef]
9. Park, S.-O.; Hong, S.; Sung, S.-J.; Kim, D.; Seo, S.; Jeong, H.; Park, T.; Cho, W.J.; Kim, J.; Choi, S. Phase-change memory via a phase-changeable self-confined nano-filament. *Nature* **2024**, *628*, 293–299.

10. Choi, C.; Leem, J.; Kim, M.; Taqieddin, A.; Cho, C.; Cho, K.W.; Lee, G.J.; Seung, H.; Bae, H.J.; Song, Y.M. Curved neuromorphic image sensor array using a MoS_2-organic heterostructure inspired by the human visual recognition system. *Nat. Commun.* **2020**, *11*, 5934. [CrossRef]
11. Zhou, T.; Lin, X.; Wu, J.; Chen, Y.; Xie, H.; Li, Y.; Fan, J.; Wu, H.; Fang, L.; Dai, Q. Large-scale neuromorphic optoelectronic computing with a reconfigurable diffractive processing unit. *Nat. Photonics* **2021**, *15*, 367–373. [CrossRef]
12. Ullman, S. Using neuroscience to develop artificial intelligence. *Science* **2019**, *363*, 692–693. [CrossRef]
13. Balamur, R.; Eren, G.O.; Kaleli, H.N.; Karatum, O.; Kaya, L.; Hasanreisoglu, M.; Nizamoglu, S. A retina-inspired optoelectronic synapse using quantum dots for neuromorphic photostimulation of neurons. *Adv. Sci.* **2024**, *11*, 2401753. [CrossRef] [PubMed]
14. Chen, Y.; Wang, H.; Chen, H.; Zhang, W.; Pätzel, M.; Han, B.; Wang, K.; Xu, S.; Montes-García, V.; McCulloch, I. Li promoting long afterglow organic light-emitting transistor for memory optocoupler module. *Adv. Mater.* **2024**, *36*, 2402515. [CrossRef]
15. Choi, W.; Shin, J.; Kim, Y.J.; Hur, J.; Jang, B.C.; Yoo, H. Versatile papertronics: Photo-induced synapse and security applications on papers. *Adv. Mater.* **2024**, *36*, 2312831. [CrossRef] [PubMed]
16. Qin, X.; Zhong, B.; Lv, S.; Long, X.; Xu, H.; Li, L.; Xu, K.; Lou, Z.; Luo, Q.; Wang, L. A zero-voltage-writing artificial nervous system based on biosensor integrated on ferroelectric tunnel junction. *Adv. Mater.* **2024**, *36*, 2404026. [CrossRef] [PubMed]
17. Li, C.; Hu, M.; Li, Y.; Jiang, H.; Ge, N.; Montgomery, E.; Zhang, J.; Song, W.; Dávila, N.; Graves, C.E. Analogue signal and image processing with large memristor crossbars. *Nat. Electron.* **2018**, *1*, 52–59. [CrossRef]
18. Liu, L.; Xu, W.; Ni, Y.; Xu, Z.; Cui, B.; Liu, J.; Wei, H.; Xu, W. Stretchable neuromorphic transistor that combines multisensing and information processing for epidermal gesture recognition. *ACS Nano* **2022**, *16*, 2282–2291. [CrossRef]
19. Li, C.; Belkin, D.; Li, Y.; Yan, P.; Hu, M.; Ge, N.; Jiang, H.; Montgomery, E.; Lin, P.; Wang, Z. Efficient and self-adaptive in-situ learning in multilayer memristor neural networks. *Nat. Commun.* **2018**, *9*, 2385. [CrossRef]
20. Guo, L.; Han, S.-T.; Zhou, Y. Electromechanical coupling effects for data storage and synaptic devices. *Nano Energy* **2020**, *77*, 105156. [CrossRef]
21. Shim, H.; Ershad, F.; Patel, S.; Zhang, Y.; Wang, B.; Chen, Z.; Marks, T.J.; Facchetti, A.; Yu, C. An elastic and reconfigurable synaptic transistor based on a stretchable bilayer semiconductor. *Nat. Electron.* **2022**, *5*, 660–668. [CrossRef]
22. Seo, S.; Jo, S.-H.; Kim, S.; Shim, J.; Oh, S.; Kim, J.-H.; Heo, K.; Choi, J.-W.; Choi, C.; Oh, S. Artificial optic-neural synapse for colored and color-mixed pattern recognition. *Nat. Commun.* **2018**, *9*, 5106. [CrossRef]
23. Wang, C.-Y.; Liang, S.-J.; Wang, S.; Wang, P.; Li, Z.A.; Wang, Z.; Gao, A.; Pan, C.; Liu, C.; Liu, J. Gate-tunable van der Waals heterostructure for reconfigurable neural network vision sensor. *Sci. Adv.* **2020**, *6*, eaba6173. [CrossRef] [PubMed]
24. Yu, J.; Yang, X.; Gao, G.; Xiong, Y.; Wang, Y.; Han, J.; Chen, Y.; Zhang, H.; Sun, Q.; Wang, Z.L. Bioinspired mechano-photonic artificial synapse based on graphene/MoS_2 heterostructure. *Sci. Adv.* **2021**, *7*, eabd9117. [CrossRef]
25. Kim, M.K.; Lee, J.S. Synergistic improvement of long-term plasticity in photonic synapses using ferroelectric polarization in hafnia-based oxide-semiconductor transistors. *Adv. Mater.* **2020**, *32*, 1907826. [CrossRef]
26. Seo, S.; Lee, J.J.; Lee, R.G.; Kim, T.H.; Park, S.; Jung, S.; Lee, H.K.; Andreev, M.; Lee, K.B.; Jung, K.S. An optogenetics-inspired flexible van der Waals optoelectronic synapse and its application to a convolutional neural network. *Adv. Mater.* **2021**, *33*, 2102980. [CrossRef]
27. Zhou, X.; Hu, F.; Hou, Q.; Hu, J.; Wang, Y.; Chen, X. All-photonic artificial synapses based on photochromic perovskites for noncontact neuromorphic visual perception. *Commun. Mater.* **2024**, *5*, 116. [CrossRef]
28. Zhang, W.; Eperon, G.E.; Snaith, H.J. Metal halide perovskites for energy applications. *Nat. Energy* **2016**, *1*, 16048. [CrossRef]
29. Schulz, P.; Cahen, D.; Kahn, A. Halide perovskites: Is it all about the interfaces? *Chem. Rev.* **2019**, *119*, 3349–3417. [CrossRef]
30. Manser, J.S.; Saidaminov, M.I.; Christians, J.A.; Bakr, O.M.; Kamat, P.V. Making and breaking of lead halide perovskites. *Acc. Chem. Res.* **2016**, *49*, 330–338. [CrossRef] [PubMed]
31. Stranks, S.D.; Snaith, H.J. Metal-halide perovskites for photovoltaic and light-emitting devices. *Nat. Nanotechnol.* **2015**, *10*, 391–402. [CrossRef]
32. Jena, A.K.; Kulkarni, A.; Miyasaka, T. Halide perovskite photovoltaics: Background, status, and future prospects. *Chem. Rev.* **2019**, *119*, 3036–3103. [CrossRef]
33. Mao, L.; Stoumpos, C.C.; Kanatzidis, M.G. Two-dimensional hybrid halide perovskites: Principles and promises. *J. Am. Chem. Soc.* **2018**, *141*, 1171–1190. [CrossRef]
34. Halder, A.; Choudhury, D.; Ghosh, S.; Subbiah, A.S.; Sarkar, S.K. Exploring thermochromic behavior of hydrated hybrid perovskites in solar cells. *J. Phys. Chem. Lett.* **2015**, *6*, 3180–3184. [CrossRef]
35. Haque, M.A.; Syed, A.; Akhtar, F.H.; Shevate, R.; Singh, S.; Peinemann, K.-V.; Baran, D.; Wu, T. Giant humidity effect on hybrid halide perovskite microstripes: Reversibility and sensing mechanism. *ACS Appl. Mater. Interfaces* **2019**, *11*, 29821–29829. [CrossRef] [PubMed]
36. Deretzis, I.; Smecca, E.; Mannino, G.; La Magna, A.; Miyasaka, T.; Alberti, A. Stability and degradation in hybrid perovskites: Is the glass half-empty or half-full? *J. Phys. Chem. Lett.* **2018**, *9*, 3000–3007. [CrossRef]

37. Leguy, A.M.A.; Hu, Y.; Campoy-Quiles, M.; Alonso, M.I.; Weber, O.J.; Azarhoosh, P.; Van Schilfgaarde, M.; Weller, M.T.; Bein, T.; Nelson, J. Reversible hydration of $CH_3NH_3PbI_3$ in films, single crystals, and solar cells. *Chem. Mater.* **2015**, *27*, 3397–3407. [CrossRef]
38. Zhu, X.; Gao, C.; Ren, Y.; Zhang, X.; Li, E.; Wang, C.; Yang, F.; Wu, J.; Hu, W.; Chen, H. High-contrast bidirectional optoelectronic synapses based on 2D molecular crystal heterojunctions for motion detection. *Adv. Mater.* **2023**, *35*, 2301468. [CrossRef] [PubMed]
39. Chen, H.; Lou, S.; Wang, Q.; Huang, P.; Hu, Y. Diffractive deep neural networks: Theories, optimization, and applications. *Appl. Phys. Rev.* **2024**, *11*, 011305. [CrossRef]
40. Feldmann, J.; Youngblood, N.; Karpov, M.; Gehring, H.; Li, X.; Stappers, M.; Le Gallo, M.; Fu, X.; Lukashchuk, A.; Raja, A.S.; et al. Parallel convolutional processing using an integrated photonic tensor core. *Nature* **2021**, *589*, 52–58. [CrossRef]
41. Lin, X.; Rivenson, Y.; Yardimci, N.T.; Veli, M.; Luo, Y.; Jarrahi, M.; Ozcan, A. All-optical machine learning using diffractive deep neural networks. *Science* **2018**, *361*, 1004–1008. [CrossRef] [PubMed]

Disclaimer/Publisher's Note: The statements, opinions and data contained in all publications are solely those of the individual author(s) and contributor(s) and not of MDPI and/or the editor(s). MDPI and/or the editor(s) disclaim responsibility for any injury to people or property resulting from any ideas, methods, instructions or products referred to in the content.